RESEARCH ARTICLE
https://doi.org/10.1071/ES22002

JOURNAL OF SOUTHERN HEMISPHERE EARTH SYSTEMS SCIENCE

A wave-driven surface circulation feature in Table Bay

Marc de Vos[A,B,*], Marcello Vichi[B,C] and Christo Rautenbach[B,D,E]

For full list of author affiliations and declarations see end of paper

*Correspondence to:
Marc de Vos
Marine Research Unit, South African Weather Service, Cape Town, Western Cape, South Africa
Email: marc.devos@weathersa.co.za

Handling editor:
Neil Holbrook

Received: 28 January 2022
Accepted: 31 January 2023
Published: 9 March 2023

Cite this:
de Vos M *et al.* (2023)
Journal of Southern Hemisphere Earth Systems Science
73(1), 60–76. doi:10.1071/ES22002

ABSTRACT

Table Bay, located in the Cape Peninsula region of South Africa, supports a variety of human and ecological interests. Notably it hosts a major port, with significant shipping and smaller maritime activity in and near the bay. Despite this, knowledge of its circulation dynamics remains cursory. In this study, surface gravity waves, particularly those with longer periods and higher wave heights such as swells, are shown to be important in driving near surface currents and establishing circulation patterns within Table Bay. A surface circulation feature, linked to large wave conditions and established by strong wave-driven flows near Robben Island, is identified and described by means of two coastal ocean model simulations. One simulation is dynamically coupled to a wave model and includes current forcing due to waves, whereas the other neglects waves. The influence of these wave-driven currents is relevant at the event scale, but also affects the monthly means of the simulation periods. Finally, the importance of including accurate surface gravity wave forcing in simulations of coastal currents, for applications of coastal models, is elucidated. This is achieved by analysing differences in the drift of a series of drogues deployed in the coupled and uncoupled simulations. Trajectories, drift speeds and drogue fates differed materially between the two configurations, underscoring the implications of wave-driven currents for common use cases.

Keywords: Cape Peninsula, circulation, coastal currents, South Africa, Table Bay, wave–current interactions, wave dynamics, wave sheltering.

1. Introduction

1.1. Geographical context

Table Bay is one of two defining embayments of the Cape Peninsula region, on the south-west coast of South Africa. The bay and surrounding area are shown in Fig. 1. Robben Island is a prominent feature of the area, lying to the north-west of the bay. Bathymetry rises sharply from depth to form Robben Island's western shores, with more gradually shallowing bathymetry along its southern and south-eastern shores. A submerged ridge connects the island to the mainland at Blouberg. Whale Rock, a small outcrop ~1.9 km south of Robben Island, breaks the surface, with a slightly shallower ridge between it and the shores of the island. Table Bay is typically defined by two bounding lines between a headland at Green Point and Robben Island, and between Robben Island and Bloubergstrand, with a predominantly north-west and west facing mouth. It covers ~100 km^2 and reaches a maximum depth of ~35 m (Quick and Roberts 1993). A rocky shoreline extends southward from Green Point, with the large commercial port located a short distance to the west of the headland. From there, largely sandy beaches extend northwards, defining the west coast and boundary of the embayment. The importance of Table Bay is multidimensional, with significant stakeholder interests in boating and shipping (Quick and Roberts 1993; Potgieter *et al.* 2020), tourism and recreation, (Quick and Roberts 1993; Ballance *et al.* 2000; Munien *et al.* 2019), and fisheries of various scales (Quick and Roberts 1993; Van Ballegooyen 2007).

1.2. Existing knowledge of the circulation

The physical oceanography of Table Bay is generally under-studied, with little information available in the literature. By the early 1990s most available information comprised

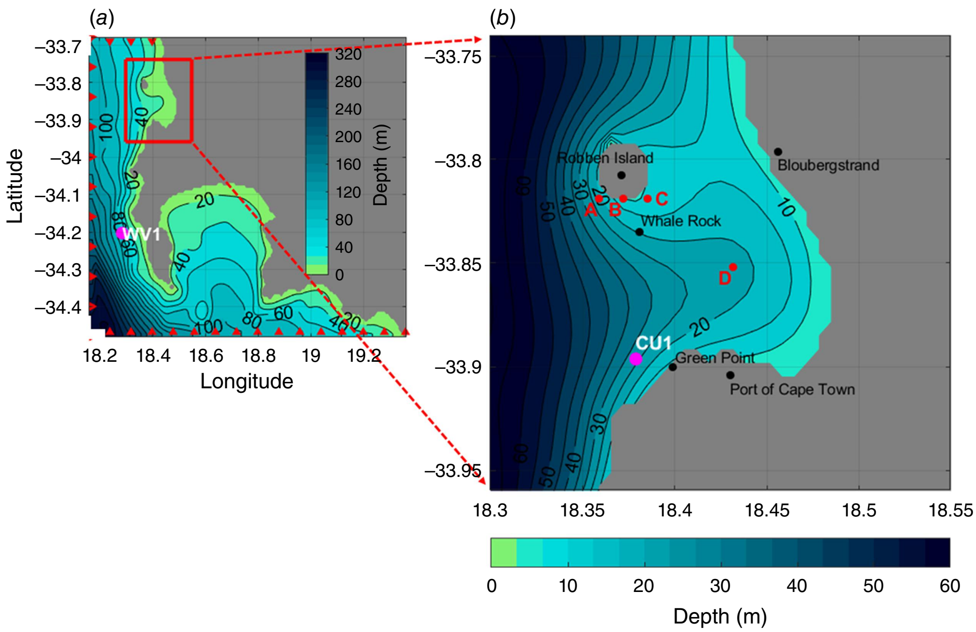

Fig. 1. (*a*) Full model domain with the focus area for this study in bounded in red. Model bathymetry is shown in colour and red markers around the boundaries indicate nodes at which boundary conditions from a global model are prescribed. (*a*) Site WV1 shows the location of the Waverider buoy used to evaluate the performance of the wave model. (*b*) A zoom of the focus area. Site CU1 indicates the location of the ADCP against whose measurements the model data were compared. Sites A–D indicate the locations at which time series were analysed in Section 3.3.

commercial reports (Quick and Roberts 1993) of a cursory nature, with little further work being conducted. Notwithstanding, the general circulation has been found to be overwhelmingly wind-driven (Van Ieperen 1971; Quick and Roberts 1993), with typical surface currents reaching speeds of 0.2–0.3 m s^{-1} (Quick and Roberts 1993). The placement of the south Atlantic anticyclone gives rise to frequent strong south-easterly winds during summer months, whereas passing midlatitude cyclones and coastal low pressures bring north-westerly winds ahead of cold fronts during winter (Jury 1984; Boyd *et al.* 1985; Tyson *et al.* 1996). These wind regimes accordingly drive a general northward and southward drift through the bay. Remote forcing and influences of far-field currents on the circulation within the bay are negligible (Van Ieperen 1971; Council for Scientific and Industrial Research 1972*a*, 1972*b*). Tides drive weak currents, given the modest tidal range of ~1.8 m at spring maximum (Van Ieperen 1971; Schumann and Perrins 1982). Surface gravity waves were noted to be the dominant forcing in the nearshore, especially along the eastern margins of the bay, where oblique wave action drives northward longshore currents (Van Ieperen 1971; Council for Scientific and Industrial Research 1972*a*). Van Ballegooyen (2007) utilised a model to investigate dredge plume dynamics near the port and presented a series of surface current field snapshots during typical wind conditions. However, the study stopped short of detailed analysis of surface currents, beyond linking to the general northward and southward drifts associated with prevailing winds and referred to in the literature. Wave-driven currents are mentioned in the context of the nearshore, but not other areas within the bay.

Further afield, Mulligan *et al.* (2008) employed the same modelling system as the one used in this study to assess the wave-driven flows in a coastal bay in south-east Nova Scotia during a hurricane. In that study, observed currents could only be satisfactorily reproduced by including wave forcing in the circulation model. Radiation stress gradients, predominantly due to breaking-induced wave energy dissipation, were shown to be important drivers of Eulerian flows. Circulation patterns within the bay were established by strong wave-induced flow along a shoreline and in the vicinity of a shoal near the mouth of the bay. Mulligan *et al.* (2010) extended this work to focus on the particular role of wave-breaking over the shoal in driving currents, with a model producing a jet current with speeds in the range of 0.4–0.7 m s^{-1}; up to four times the magnitude of currents in the absence of wave forcing. These magnitudes were slightly over-predicted relative to observations but were accurate in direction and timing, and highlight the importance of wave forcing in simulating coastal currents, particularly during large wave events. Rey and Mulligan (2021) also utilised Delft3D Flow and SWAN to simulate the coastal hydrodynamics near a stretch of North Carolina shoreline during a hurricane. Although the focus of that study was on the effect of different wind forcing on the quality of the simulations, the authors also noted the importance of wave forcing on currents in certain parts of their domain, especially during large wave events.

This study demonstrates that large wave events drive Eulerian circulation features within Table Bay which dominate the circulation at the event scale and modify the mean flow. Further, it shows the importance of including surface gravity wave forcing in any assessment of the circulation within Table Bay.

2. Materials and methods

2.1. Numerical models

The numerical models employed in this study were built in the Delft3D modelling environment, with Delft3D FLOW (Lesser *et al.* 2004) and SWAN (Booij *et al.* 1999) providing hydrodynamic and wave simulations respectively. Delft3D FLOW solves the unsteady Reynolds averaged Navier Stokes equations in three dimensions (3-D) (Lamb 1993). This modelling system was selected due to its well-established reliability (Roelvink and Van Banning 1995; Elias *et al.* 2000; Gerritsen *et al.* 2008) and its extensive use in coastal ocean modelling projects (Putzu *et al.* 2019). It has been applied throughout the world in coastal contexts similar to this one (e.g. Mulligan *et al.* 2008, 2010; Garcia *et al.* 2015; Hasan *et al.* 2016; Peng and Bradon 2016; de Mendoza *et al.* 2018; Rey and Mulligan 2021). Recent coupled Delft3D FLOW/SWAN configurations have also been successfully applied to this study region by Barnes and Rautenbach (2020), de Vos *et al.* (2021) and Rautenbach *et al.* (2020*b*). The reader is referred to Lesser *et al.* (2004) for a full description of Delft3D FLOW. SWAN is a third generation spectral wave model that has been successfully applied to a variety of coastal problems (Booij *et al.* 1999; Ris *et al.* 1999; Zubier *et al.* 2003; Rogers *et al.* 2007; Thomas and Dwarakish 2015). Delft3D SWAN configurations have been recently applied to this study region (Rautenbach *et al.* 2020*a*; Daniels *et al.* 2022). In this study, two configurations are employed. The first is a fully coupled configuration of Delft3D FLOW and SWAN, enabling two-way wave–current interactions. The handling of wave–current interactions by the model is outlined in Section 2.1.4. The second is a configuration of Delft3D FLOW with no wave coupling, but identical in all other respects to the first. The models were calibrated and validated by iterative tuning of one parameter setting at a time, according to the methodology proposed by Williams and Esteves (2017). Two simulations periods of 3 months each were used. These periods, August–October in 2006 and 2010, were selected based on the best overlap of available observations for use in calibration and validation of the overall model domain (i.e. not just the Table Bay sub-domain considered here). The final model parameter settings can be found in Table 1.

2.1.1. Model grid and bathymetry

The Delft3D FLOW and SWAN models are discretised on identical regular curvilinear grids with a horizontal resolution varying between 600 and 700 m. Ten sigma layers

Table 1. Summary of numerical model parameter settings used in the study.

Parameterisation	Model	Coefficient
Circulation model (Delft3D FLOW ver. 6.03.00)		
Bottom roughness	Chézy (quadratic friction law)	$C_{2D} = 65$ (u), $C_{2D} = 15$ (v)
Wind drag breakpoint coefficients	Sembiring *et al.* (2015)	$U_{10} = 0\ \mathrm{m\ s^{-1}}$, $100\ \mathrm{m\ s^{-1}}$ $C_D = 0.63 \times 10^{-3}$, 7.23×10^{-3}
Background horizontal eddy viscosity	–	$10\ \mathrm{m^2\ s^{-1}}$
Background vertical eddy viscosity	–	$1 \times 10^{-6}\ \mathrm{m^2\ s^{-1}}$
Background horizontal eddy diffusivity	–	$10\ \mathrm{m^2\ s^{-1}}$
Background vertical eddy diffusivity	–	$1 \times 10^{-6}\ \mathrm{m^2\ s^{-1}}$
Turbulence closure model	k-L	
Secchi depth	Ocean	2.0 m
Stanton number	Ocean	1.3×10^{-3}
Dalton number	Ocean	1.7×10^{-3}
Wave model (SWAN v40.72)		
Bottom friction	Madsen *et al.* (1988)	$K_n = 0.05$
Depth-induced breaking	Battjes and Janssen (1978)	Alpha (dissipation) = 1
		Gamma (breaker) = 0.73
White-capping	van der Westhuysen (2007)	

were employed in the vertical, with higher resolutions at the surface and near the bed. The computational time step was set to 0.75 s to satisfy Courant–Friedrichs–Lewy considerations. Composite bathymetry was assembled by combining General Bathymetric Chart of the Oceans data with a resolution of 1' with high resolution soundings provided by the South African Navy Hydrographic Office (SANHO) and interpolated to the model grid as shown in Fig. 1.

2.1.2. Open boundary conditions

Temperature, salinity, velocity and water surface elevation conditions (including tide and meteorologically driven contributions) are prescribed at the open horizontal and vertical Delft3D FLOW model boundaries and updated 3-hourly at the points indicated in Fig. 1*a*. These data are obtained from the Global Ocean Forecasting System (ver. 3.1) reanalysis product (Metzger *et al.* 2017) of the US Naval Research Laboratory: Ocean Dynamics and Prediction Branch (see https://www.hycom.org/dataserver/gofs-3pt1/reanalysis, accessed 26 June 2020), with a horizontal resolution of 0.08°. Velocities and surface elevations are prescribed as Riemann-type boundary conditions (Stelling 1983). This configuration was recently successfully employed for a similar use case by Rey and Mulligan (2021). The SWAN model was prescribed non-spectral, parameter wave boundary conditions from the National Centers for Environmental Prediction operational forecast model (WaveWatch III, see https://www.ncei.noaa.gov/thredds-ocean/catalog/ncep/nww3/2006/10/glo_30m/catalog.html). Parameters were prescribed with a horizontal resolution of 0.5°, assuming a JONSWAP spectrum (Battjes *et al.* 1986). This approach was deemed effective for this geographical setting by Rautenbach *et al.* (2020*a*), who nevertheless showed moderate improvement with fully spectral boundary conditions. It has also been recently deployed successfully in the area by Daniels *et al.* (2022). Since the study domain is located far from model boundaries and the high-resolution wind forcing thereby given sufficient fetch to realistically influence local wind seas, it is presumed that remote swell is the most important part of the incoming wave spectrum to capture at the boundaries (in this domain, usually represented by the peak period). The single-peaked JONSWAP assumption is suitable in this case, as can be verified during model evaluation. Veitch *et al.* (2019) point out that upon reaching the south-west coastline of South Africa, the incoming wave energy spectrum has narrowed significantly, with swell dominating. Still, where complex sea states with additional spectral peaks (e.g. wind seas) are significant enough to affect the study domain deep within the model grid, the single-peak limitation may cause deficiencies.

2.1.3. Atmospheric and tidal forcing

Hourly wind forcing with a horizontal resolution of 0.03° (~3 km) from the Wind Atlas of South Africa (WASA) (Hahmann *et al.* 2014) was applied to the circulation and wave models. The WASA data were produced by a downscaling of the ERA-Interim (ERA-I) reanalysis product (Dee *et al.* 2011) using the Weather Research and Forecasting model (Skamarock *et al.* 2008). Hourly sea-level pressure, temperature at 2 m above sea level, total cloud cover and dew point temperature data from ERA-I were also used. The ERA-I has a horizontal resolution of ~79 km but is also provided at ~13.9-km resolution (used here) from the bi-linear interpolation technique of the European Centre for Medium-Range Weather Forecasts. Sea-level pressure is included to account for the inverse barometric effect on sea level. The temperature variables, relative humidity (derived from temperature variables) and total cloud cover are used to compute surface heat fluxes using Delft3D's ocean heat flux model, following Gill (1982) and Lane (1989). Newtonian gravitational (tidal) forcing of the water mass within the model is accounted for by the most significant semi-diurnal, diurnal and long-period harmonic constituents (11 in total).

2.1.4. Modelling of wave–current interactions

Delft3D can simulate two-way wave–current interactions. Wave-induced current forcing in the model is based on gradients of radiation stresses. Radiation stresses can be thought of as excess flows of momentum as a result of the presence of waves (Longuet-Higgins and Stewart 1964). Wave breaking in particular, a mechanism of wave energy dissipation, can transfer momentum to the Eulerian flow by gradients in radiation stress according to Eqn 1 (Longuet-Higgins and Stewart 1964):

$$(F_x, F_y) = -\left(\frac{\partial S_{xx}}{\partial x} + \frac{\partial S_{xy}}{\partial y}, \frac{\partial S_{yx}}{\partial x} + \frac{\partial S_{yy}}{\partial y}\right) \quad (1)$$

where F is the wave-induced force in the x and y directions and S is the radiation stress tensor. The radiation stress tensor is two-dimensional (2-D) to depth-averaged simulations (Nguyen *et al.* 2021) or situations where the mean motion is uniform with depth (Deltares 2020*a*). It is applied to the surface layer in 3-D configurations (Cats 2014). Sensitivity testing between 2-D and fully 3-D configurations, and comparisons of depth-averaged currents against surface currents revealed that the development of the circulation feature, on which this study is focused, was unaffected. This is likely due to the shallow bathymetry and barotropic conditions in the area. Accordingly, the fully 3-D model is used.

For 3-D implementations, wave-induced force is better approximated from wave energy dissipation (Eqn 2) than radiation stress directly. This finding is explained in detail by Dingemans *et al.* (1987) and is the approach adopted in this study:

$$(F_x, F_y) = \left(D\frac{k_x}{\omega}, D\frac{k_y}{\omega}\right) \quad (2)$$

where ω is the fixed wave frequency, k is the wave number and D is the rate of wave energy dissipation, computed internally in SWAN as the sum of energy dissipation due to depth-induced breaking (S_{brk}), whitecapping (S_{wc}) and bottom friction (S_{bot}) per unit time (Cats 2014). The energy dissipation rate due to breaking is determined using Eqn 3 (Battjes and Janssen 1978):

$$D_{tot} = -\frac{1}{4}\alpha_{BJ} Q_b \left(\frac{\bar{\sigma}}{2\pi}\right) H_{max}^2 \quad (3)$$

where $\alpha_{BJ} = 1$, $\bar{\sigma}$ is the mean relative wave frequency, Q_b is the breaking wave fraction and H_{max} is the maximum possible wave height for a given depth according to:

$$H_{max} = \gamma h$$

where h is water depth and γ is the depth induced breaking parameter and set to 0.73, following Battjes and Stive (1985) and Deltares (2020*b*). In 3-D configurations, the three dissipation modes (S_{brk}, S_{wc} and S_{bot}) are handled separately in order to account for their effects on the vertical appropriately: S_{brk} and S_{wc} affect the surface and S_{bot} affects the bed layer. Delft3D does not explicitly consider the presence of waves in modifying surface wind stress due to surface roughness. Rather, roughness is considered by a constant adjustment of wind drag (C_D in Table 1) as a function of wind speed. For a full description of the wave–current interaction formulation, the reader is referred to Deltares (2020*a*). In Delft3D, momentum due to Stokes drift is added to flow velocities by writing and solving the hydrodynamic equations in a Generalised Lagrangian Mean (GLM; Andrews and Mcintyre 1978) formulation (Deltares 2020*a*). The relationship between the so-called GLM (or total), Eulerian and Stokes drift velocities is given by Eqn 4:

$$\vec{u}^L = \vec{u}^E + \vec{u}^S \quad (4)$$

where $\vec{u}^L$, $\vec{u}^E$ and $\vec{u}^S$ are the GLM velocity, Eulerian and Stokes drift vectors respectively (Deltares 2020*a*). This study is concerned with the wave-induced contribution to the Eulerian, or mean flow, so results and discussions in subsequent sections relate to $\vec{u}^E$.

2.2. Observations

Measurements of significant wave height (H_s), peak wave period (T_p) and peak direction (D_p) from a Datawell Waverider buoy located at Slangkop were utilised to assess performance of the wave model at a co-located point. The buoy is located ~40 km south-southwest of Table Bay (34.204°S, 18.2876°E, indicated by point WV1 in Fig. 1*a*) and provides a good representation of the wave regime reaching the peninsula region prior to refraction and shoaling into Table Bay. Velocity measurements from an Acoustic Doppler Current Profiler (ADCP) were utilised to assess the reproduction of the near-surface currents by the model. The instrument was located near Green Point (33.8962°S, 18.3787°E, indicated by point CU1 in Fig. 1*b*). Given the sigma vertical coordinates employed by the model, near-surface velocities from the second layer were extracted, corresponding to a mean sea level depth of 4.4 m.

For a comprehensive summary of the calibration and validation of the modelling system, the reader is referred to de Vos *et al.* (2021), with the present configuration differing only in its boundary forcing type. More specifically, the previous version used astronomic water-level boundary conditions, whereas the present implementation uses Riemann condition as explained in Section 2.1.2 (though the results were largely insensitive to this change).

3. Results and discussion

3.1. Model assessment

3.1.1. Wave simulations

Comparisons between modelled data and measurements from the Slangkop Waverider buoy indicate good agreement. The model was able to reproduce the mean wave conditions for 3-month simulation periods, as well as the sub-daily variability. During August–October 2006, mean modelled (measured) H_s, T_p and D_p of 2.80 m (2.61 m), 11.88 s (12.24 s) and 225.0° (228.4°) respectively were obtained. For 2010, mean modelled (measured) H_s, T_p and D_p were 2.64 m (2.42 m), 11.16 s (11.08 s) and 227.1° (231.0°) respectively. Hourly root mean squared errors (RMSEs) were computed to assess the model's ability to reproduce sub-daily variability. The RMSEs for H_s, T_p and D_p of 0.5 m, 1.42 s and 10.85° were obtained for the 2006 period, and 0.52 m, 1.6 s and 19.4° for the 2010 period. Fig. 2 shows the model's ability to reproduce the wave parameter distributions in the vicinity of the area of interest. The alignment of the red and green lines joining the first and third quartiles of each variable distribution in the quantile–quantile plots indicates that the model correctly simulates the majority of the distribution. The model also correctly reproduces the timing, magnitude and direction of wave events, with significant wave heights in 2006, and peak wave periods in 2010 for very large events (75th percentile and beyond) slightly underestimated.

3.1.2. Current simulations

The acute lack of available measurements for comparison of current velocities challenges the robust evaluation of the model's performance. Despite the known limitations of satellite altimetry derived velocity data near the coast (Benveniste *et al.* 2020), its potential for model evaluation was investigated. The available gridded products provided wholly insufficient coverage and resolution of Table Bay, however. Therefore, point-validation was performed against available data from the ADCP near Green Point (point CU1 in Fig. 1*b*). In this regard, the model reproduced the mean and sub-daily circulation variability for the 2006 simulation (for which measurements were available). During August–October 2006,

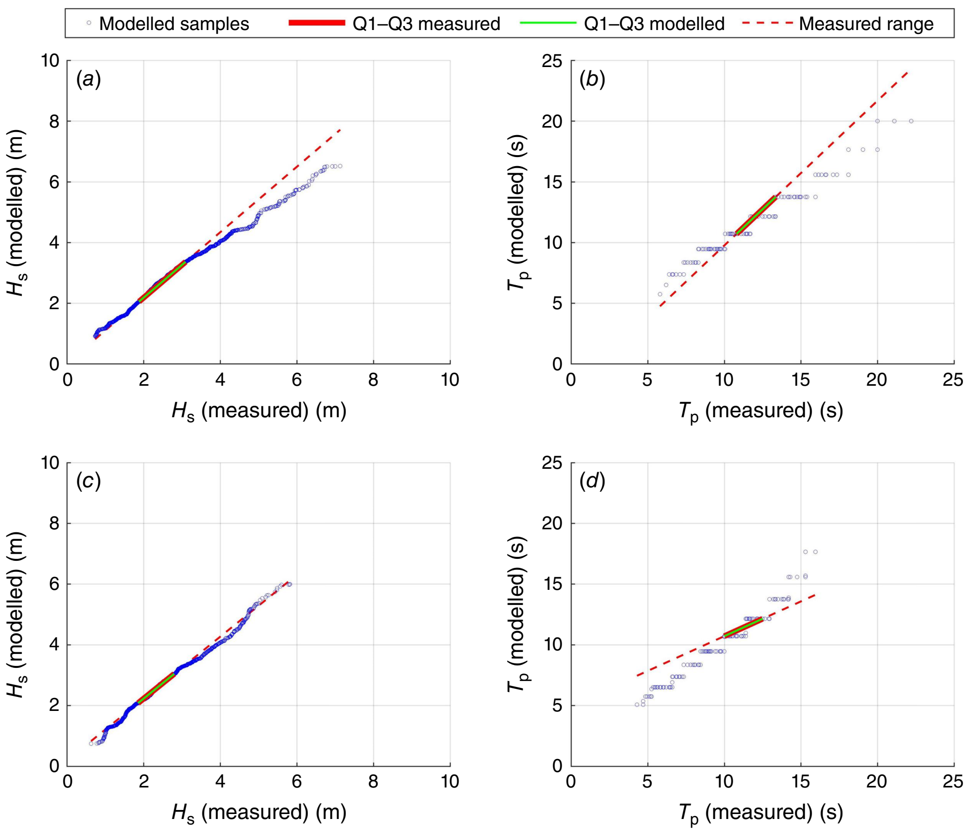

Fig. 2. Quantile–quantile plots for significant wave height and peak wave period for the periods in (*a*, *b*) 2006 and (*c*, *d*) 2010 respectively. Blue markers are modelled samples. The solid red and green lines join the first (Q1) and third (Q3) quartiles of the measured and modelled distributions respectively. The red dashed line is an extrapolation of the Q1–Q3 measured line to the ends of the data.

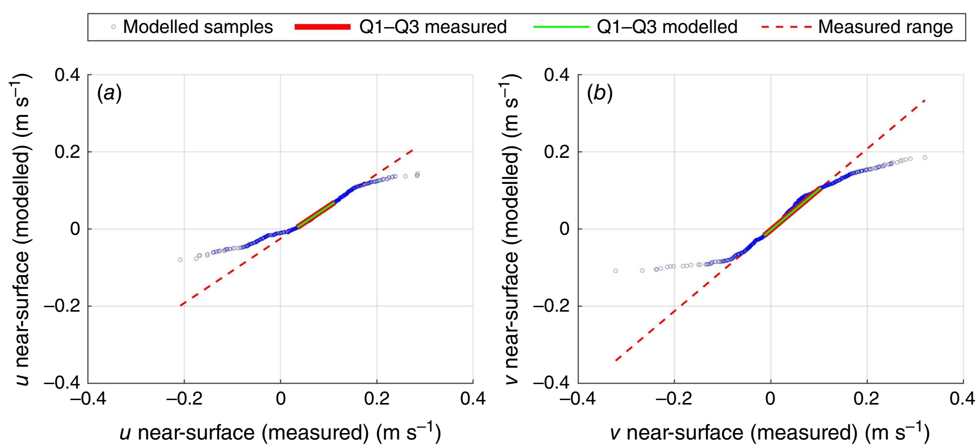

Fig. 3. Quantile–quantile plots for near-surface (*a*) *u* and (*b*) *v* flow components for the 2006 period. Blue markers are modelled samples. The solid red and green lines join the first (Q1) and third (Q3) quartiles of the measured and modelled distributions respectively. The red dashed line is an extrapolation of the Q1–Q3 measured line to the ends of the data.

mean modelled (measured) u and v velocity components of 0.057 (0.080) m s^{-1} and 0.060 (0.083) m s^{-1} respectively were obtained. The RMSEs for u and v of 0.08 and 0.10 m s^{-1} respectively were obtained. Fig. 3 shows the model's ability to reproduce the surface current distributions near the area of interest. The alignment of the lines joining the first and third quartiles of each variable distribution in the quantile–quantile plots indicates that the model correctly reproduces the majority of the distribution. Very strong eastward and strong westward flow components are slightly underestimated. The same applies to strong northward and southward flow components. This consistent underestimation of very strong or weak flows could be due to insufficient mixing in the hydrodynamic model. For example, although dissipation due to depth-induced breaking, whitecapping and friction is considered, low-frequency swell dissipation, which can affect orbital motion in lower layers, is not. For more comprehensive information on calibration and validation, the reader is referred to de Vos *et al.* (2021). The development of the circulation patterns discussed in Section 3.2 was found to be insensitive to the choice of boundary forcing configuration (with astronomic water level and Riemann types having been tested) and parameter settings (such as bottom roughness and bottom wave stress formulations and coefficients), with these choices affecting mainly wave and current vector accuracies.

3.2. Gyre driven by large wave events

Inspection of surface current fields revealed interesting spatial patterns during episodes of intense wave conditions. Specifically, a cyclonic gyre, centred to the south-east of Robben Island, was noted to develop in response to large wave conditions west of the island. This feature was first noted by de Vos *et al.* (2021) but not investigated in detail. The feature had its strongest flow in its north-west quadrant, nearest the south-eastern shores of Robben Island where the bathymetry shoals between the island and Whale Rock. This appears to be a similar forcing mechanism to that driving the wave-driven jet current investigated by Mulligan *et al.* (2010). Strong flow also developed between Robben Island and the mainland at Bloubergstrand. Near Bloubergstrand, the strong westward and north-westward flow associated with the gyre became bifurcated, splitting into northward and southward alongshore components. The gyre developed on 10 occasions during the 2006 period and five occasions during the 2010 period. Key details of the surface characteristics associated with each occurrence are given in Table 2. Although not a core focus of the present study, the vertical velocity structure of the gyres was briefly investigated and found to be homogenous throughout the water column. This is to be expected, given the established importance of wave and, to a lesser extent, wind forcing in this area, combined with the shallowness of the bay. The development of the gyre appears independent of wind, occurring similarly during different wind conditions, and persisting through changes thereto. This strengthened the hypothesis that the feature is wave-driven. To confirm this, twin wave-coupled and -uncoupled configurations were run for each period, being identical in all other respects. This experiment confirmed that the gyre is wave-driven and also that waves are responsible for, in some cases, the significant modification of the Eulerian flow elsewhere in the bay. Fig. 4–6 show snapshots of wave and surface current parameters for times at which the three strongest cases of the gyre are at their peaks. Surface currents from both the wave-coupled and -uncoupled simulations are shown, with the most striking difference being the absence of the gyre feature and generally lower flow velocities in the uncoupled simulation. In each case, the uncoupled simulation shows surface currents responding to the wind (not shown) as expected

Table 2. Details of occurrences of the wave-driven gyre feature.

Start date	Peak	End date	$U_{ns\ max}$	H_s
2006-08-14 10:00	2006-08-15 13:00	2006-08-16 09:00	0.7	5
2006-08-16 10:00	2006-08-17 04:00	2006-08-18 10:00	0.6	4
2006-08-18 11:00	2006-08-18 20:00	2006-08-19 14:00	0.5	4
2006-08-28 16:00	2006-08-29 10:00	2006-08-31 07:00	1.0	6
2006-09-15 20:00	2006-09-16 06:00	2006-09-17 13:00	0.5	3.5
2006-09-19 01:00	2006-09-20 07:00	2006-09-22 01:00	0.6	3.5
2006-09-23 07:00	2006-09-23 22:00	2006-09-26 04:00	0.5	3.5
2006-09-28 13:00	2006-09-29 01:00	2006-09-30 07:00	0.4	2.5
2006-10-08 04:00	2006-10-09 10:00	2006-10-10 04:00	0.9	5.5
2006-10-30 01:00	2006-10-30 16:00	Simulation ends	0.4	3
2010-08-22 06:00	2010-08-23 22:00	2010-08-24 13:00	0.6	4
2010-09-10 22:00	2010-09-11 10:00	2010-09-12 04:00	0.6	4
2010-09-23 19:00	2010-09-24 10:00	2010-09-24 16:00	0.6	4
2010-10-10 21:00	2010-10-11 10:00	2010-10-12 16:00	0.9	6
2010-10-21 13:00	2010-10-21 23:00	2010-10-23 13:00	0.7	5

Start dates are defined based on the time at which a closed cyclonic circulation formed, and end dates are defined according to when this closed circulation broke down, or the high flow velocities associated with the gyre dissipated. The peak is defined based on the time at which the gyre exhibited maximum flow velocity. Maximum flow speeds attained within the gyre and significant wave height are also provided.

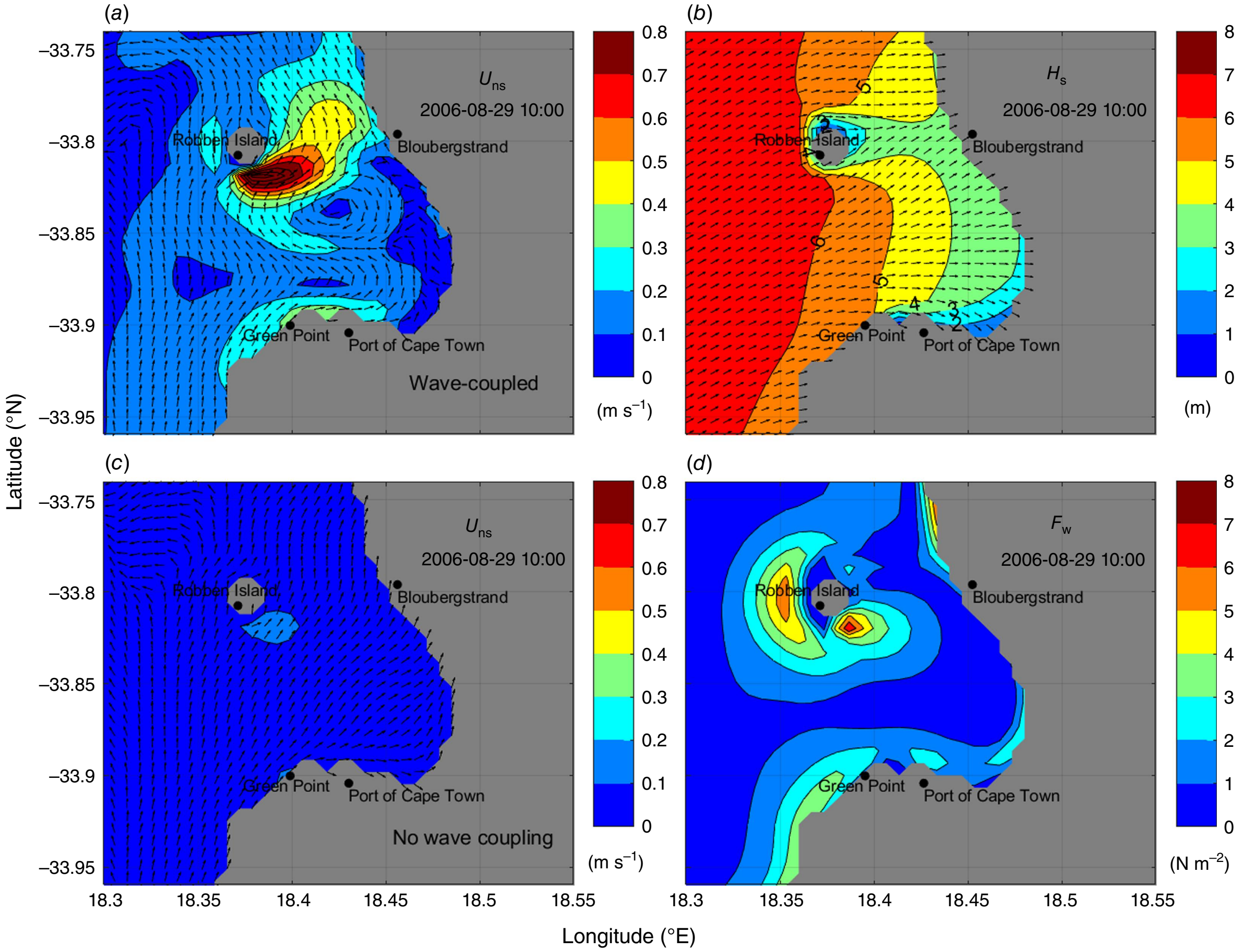

Fig. 4. Snapshot of near-surface mean current speed and direction (U_{ns}) for the (*a*, *c*) wave-coupled and -uncoupled simulations, (*b*) significant wave height (H_s) and mean wave direction and (*d*) at wave-induced force (F_w) during the peak of the first of three strong occurrences of the wave-driven gyre.

from the literature: general southward flow through Table Bay during times of northerly component winds and general northward flow in response to southerly component winds. The gyre does not develop at any stage in the uncoupled simulations but reliably occurs shortly after the onset of increasing wave energy west of Robben Island in the wave-coupled simulations. In each such case, significant wave heights of at least 2.5 m (but more often >3.5 m) propagate towards Table Bay from the west. Reasonably high wave energy dissipation rates, and consequent strong wave-induced forcing, are evident along the southern and south-eastern shores of Robben Island, north of Bloubergstrand and, to a lesser degree, at Green Point.

The topographical role of Robben Island and the shallow ridge between the island and the mainland at Bloubergstrand was briefly investigated. Two further experiments were run for the wave-coupled and -uncoupled configurations by artificially adjusting the model bathymetry. In the first, the island was smoothed out and the 15-m contour extended to enclose its area. In the second, the island and the shallow ridge were smoothed out completely, leaving no irregularities in the bay seafloor. As expected, the gyre did not develop in any of the uncoupled experiments, nor in any of the cases with the island and shallow ridge were completely removed. In the wave-coupled case with Robben Island smoothed, however, the gyre developed during large wave events ($H_s \approx$ 5–6 m) similarly to the way it did given normal bathymetry, with slightly lower maximum flow speeds near the island and slightly higher flow speeds developing north of Bloubergstrand. This suggests that it could be the largest waves in the spectrum breaking and interacting with the shallow ridge, which are predominantly responsible for the high flow speeds near the island, since with $H_s \approx$ 5–6 m, waves with heights approaching H_{max} would still be breaking in 15-m depth. Smaller waves, which would otherwise have broken near the island (thereby dissipating energy), are permitted to propagate further, ultimately breaking near Bloubergstrand, and driving higher current speeds there. During less intense cases of the gyre with lower wave conditions $H_s \approx 2.5$ m, the cyclonic pattern did develop in the case

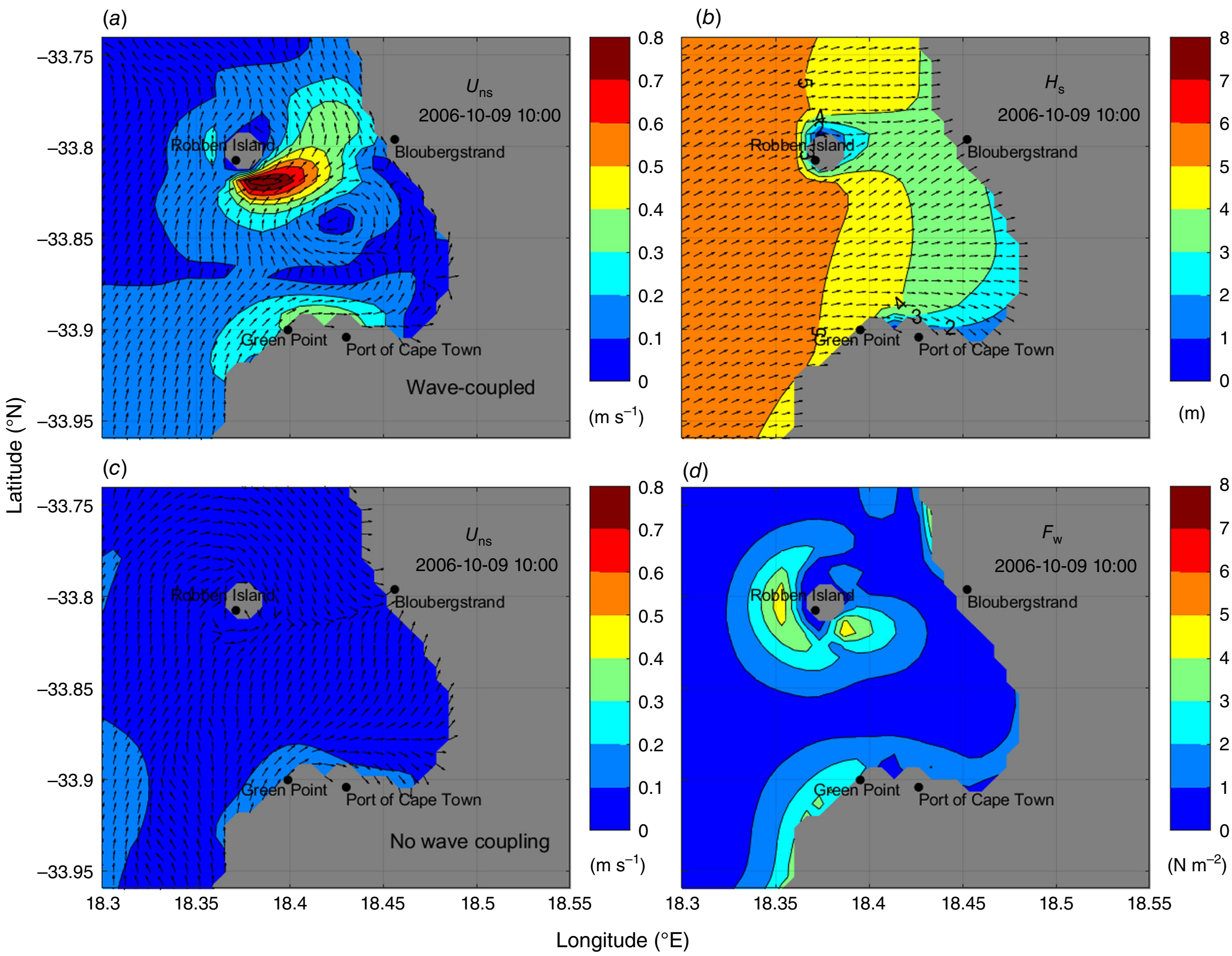

Fig. 5. Snapshot of near-surface mean current speed and direction (U_{ns}) for the (*a*, *c*) wave-coupled and wave-uncoupled simulations, (*b*) significant wave height (H_s) and mean wave direction and (*d*) wave-nduced force (F_w) during the peak of the second of three strong occurrences of the wave-driven gyre.

of the smoothed bathymetry, but there was little to no acceleration in current speeds ($U_{ns\,max} \approx 0.2\,\mathrm{m\,s^{-1}}$) as occurred in the presence of the island. This is expected, since depth-induced breaking is unlikely to be in operation for a spectrum of this nature in depths of ~15 m.

Given the scarcity of *in-situ* observations in Table Bay and the lack of coverage by either satellite-derived products or coastal observing systems such as high-frequency RADAR, there are no existing direct observations of this feature. The development of the feature in this modelling study, and its persistence throughout the model tuning process, strengthens the motivation for the enhancement of observational capacity within the bay.

To illustrate the relevance of these findings for applied problems such as search and rescue trajectory modelling, an array of virtual drogues was deployed in the coupled and uncoupled simulations. The array consisted of 55 regularly spaced drogues. The number of drogues and array spacing was designed to provide complete coverage of Table Bay given the model's horizontal resolution. They were released at the onset of each gyre event and terminated when gyres were deemed to have broken down (as per the dates listed in Table 2). Fig. 7 shows select drogue tracks which elucidate the influence of wave-driven currents on trajectories. The points along the tracks indicate 3-hourly positions. Accordingly, differences in drift speed (spacing of points) and trajectory can be inferred for drogue pairs. Key findings to emerge were, first, that the inclusion or exclusion of waves made a material, and often drastic difference to the drift trajectories of drogues released at the same point in space and time. In many cases, the divergence in trajectories was sufficiently large to make the likelihood of detection unlikely in, for example, a search and rescue context. Generally, including wave forcing increased the magnitude of the surface currents and, by extension, the drift speeds of drogues. This is evident in the wider spacing of the 3-hourly position points along each trajectory line. Second, several drogues became entrained in each of the wave-driven gyres and

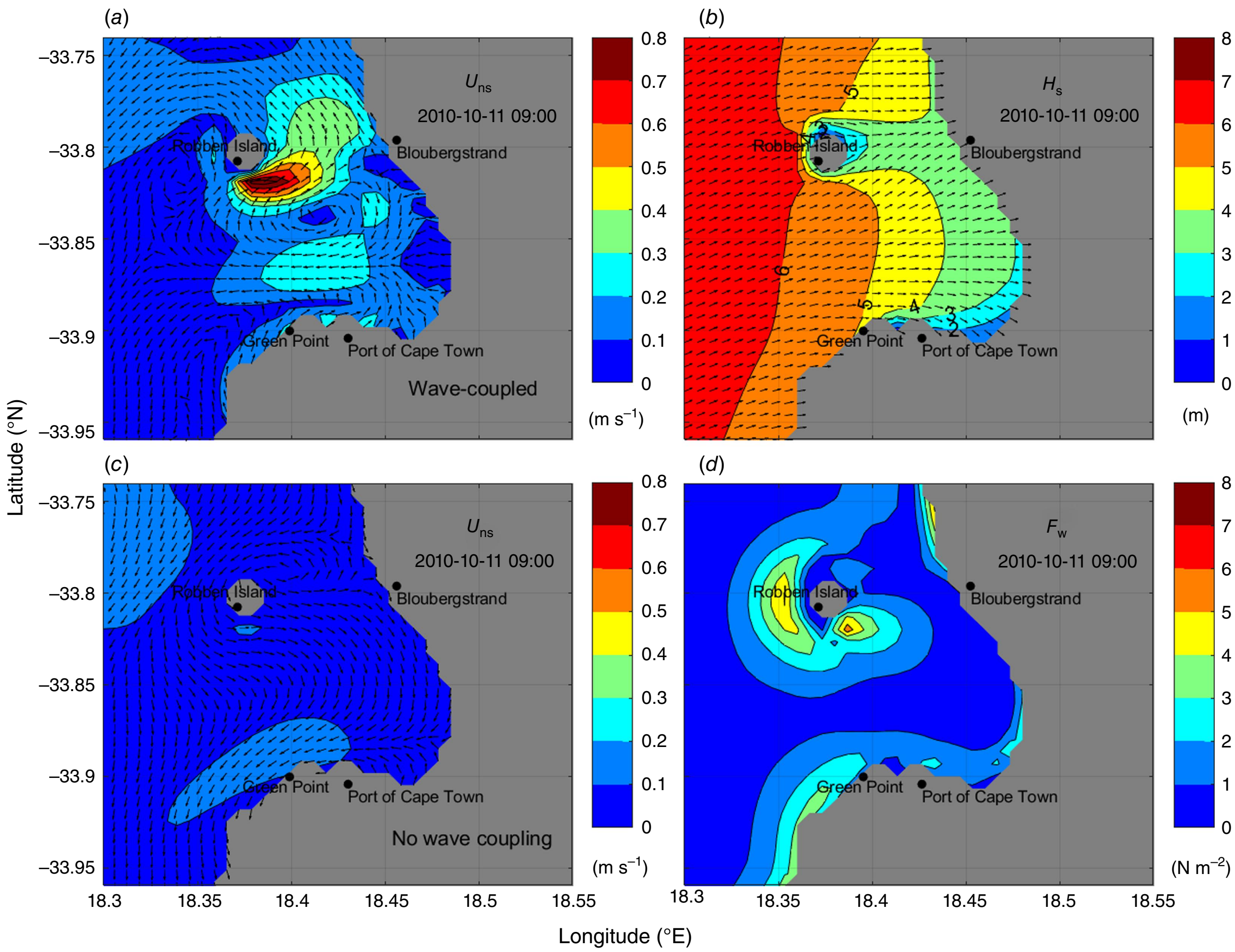

Fig. 6. Snapshot of near-surface mean current speed and direction (U_{ns}) for the (*a*, *c*) wave-coupled and wave-uncoupled simulations, (*b*) significant wave height (H_s) and mean wave direction and (*d*) wave-induced force (F_w) during the peak of the third of three strong occurrences of the wave-driven gyre.

remained so for considerable periods of time (often close to the lifetime of the gyre), before ultimately continuing in a generally northward or southward direction. This is visible in the circular drift trajectories and the number of position points along these parts of the trajectories.

Further relevance of the implications of these findings lies in the context of maritime safety. With considerable boating and shipping traffic of both a recreational and commercial nature operating in Table Bay, accurate marine weather and ocean forecasting are important (de Mey *et al.* 2009; Fossati and Piedra-Cueva 2013; de Vos *et al.* 2021). Although the effect of surface gravity waves as a risk factor to maritime activity has been established (de Vos and Rautenbach 2019), the direct effect of surface ocean currents is less clear. Anecdotally, it has been noted that ocean currents play a role in the efficiency of maritime operations near the port (Potgieter *et al.* 2020), and currents in and approaching the port have been assessed with models designed to suit engineering purposes (Van Ballegooyen 2007). However, the ability to model, and later forecast surface currents which might affect smaller vessel traffic beyond the port, by including the full range of relevant forcing, is also important (Jones and Olsonbaker 2005; Swett *et al.* 2011). For example, interactions between the surface currents driven by wave energy dissipation near Robben Island (which are insensitive to local wind direction) and locally generated wind-waves, could cause wave steepening when the currents and waves are opposed in direction (Barnes and Rautenbach 2020) and accordingly a severe sea state. Sea state is an important consideration for much activity in the bay, with the combination between wind and waves shown to cause several safety incidents in Table Bay (de Vos and Rautenbach 2019). Severe sea state also caused a high profile incident in 2017, during which a passenger ferry carrying 70 people from Robben Island to Cape Town became critically damaged, necessitating a mass rescue operation (Anxusani 2017). Factors impinging on vessel navigation such as sea state and wave steepness are not typically reported in forecasts, or sometimes even available from model output. Thus, information on parameters,

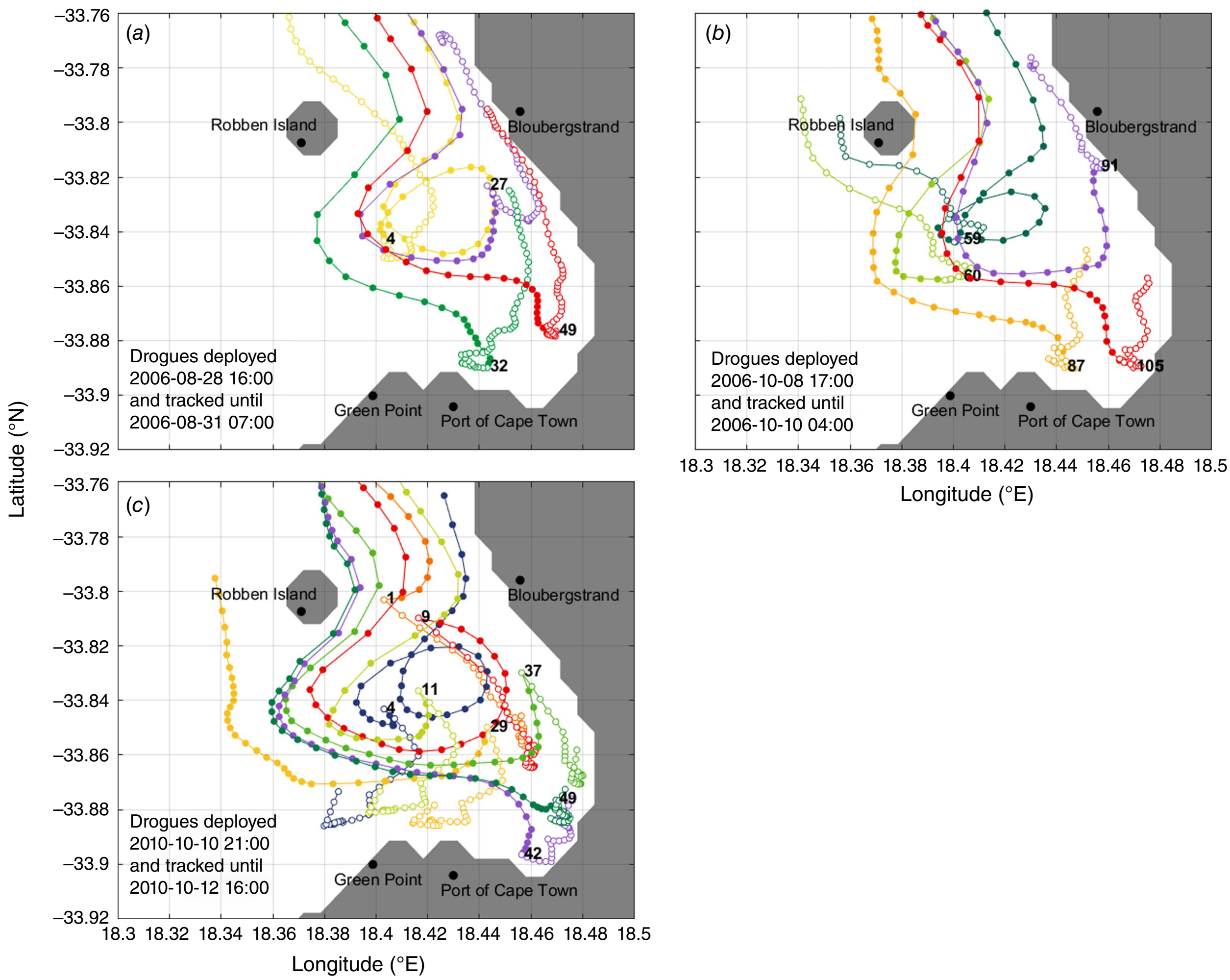

Fig. 7. Selected drogue tracks from the array of drogues deployed in model velocity fields at the onset of each of (*a*–*c*) three strong cases of the wave-driven gyre, and terminated when the features broke down. Corresponding drogue tracks in the coupled and uncoupled simulations share colours and are deployed at the same point in space and time. Drogue IDs are indicated by black text at the deployment position. Markers indicate 3-hourly positions. Drogues deployed in the coupled (or uncoupled) simulation are indicated by closed (or open) position markers.

such as wind, waves and surface currents remain important in enabling interpretation and decision making in respect of safe navigation.

3.3. Wave-induced forces driving near-surface currents

The importance of local winds in driving the surface circulation in Table Bay is well established (Van Ieperen 1971; Quick and Roberts 1993). However, the development of the circulation patterns discussed in Section 3.2 highlighted an important relationship between currents and waves, with the influence of winds apparently reduced at times within the bay. In particular, circulation features established due to strong Eulerian flow near Robben Island exhibited a predictable pattern with the approach of large waves from the open ocean to the west, ultimately governing the pattern in much of the bay. Correlation analysis was performed for points near the island and in the middle of the bay to elucidate the relationships at play between current velocity and various wave properties. Fig. 8 shows the relationships between surface current speeds for a point immediately south-east of Robben Island (point C, Fig. 1) and a range of wave properties, which were assessed for both simulation periods. Significant wave height (H_s) and mean spectral wave length ($\bar{\lambda}$) were assessed at a point 2.4 km to the west (point A, Fig. 1; in order to correlate with incident wave properties prior to nearshore transformation, thereby elucidating preconditions). Wave-induced force (F_w) and wave-energy dissipation rate (D) were assessed at a point where these waves begin breaking (point B, Fig. 1). Times at which the gyre events discussed in Section 3.2 and listed in Table 2 were at their peak are indicated by green dashed lines. Wave-induced forces explain ~90% (85%) of the variance in

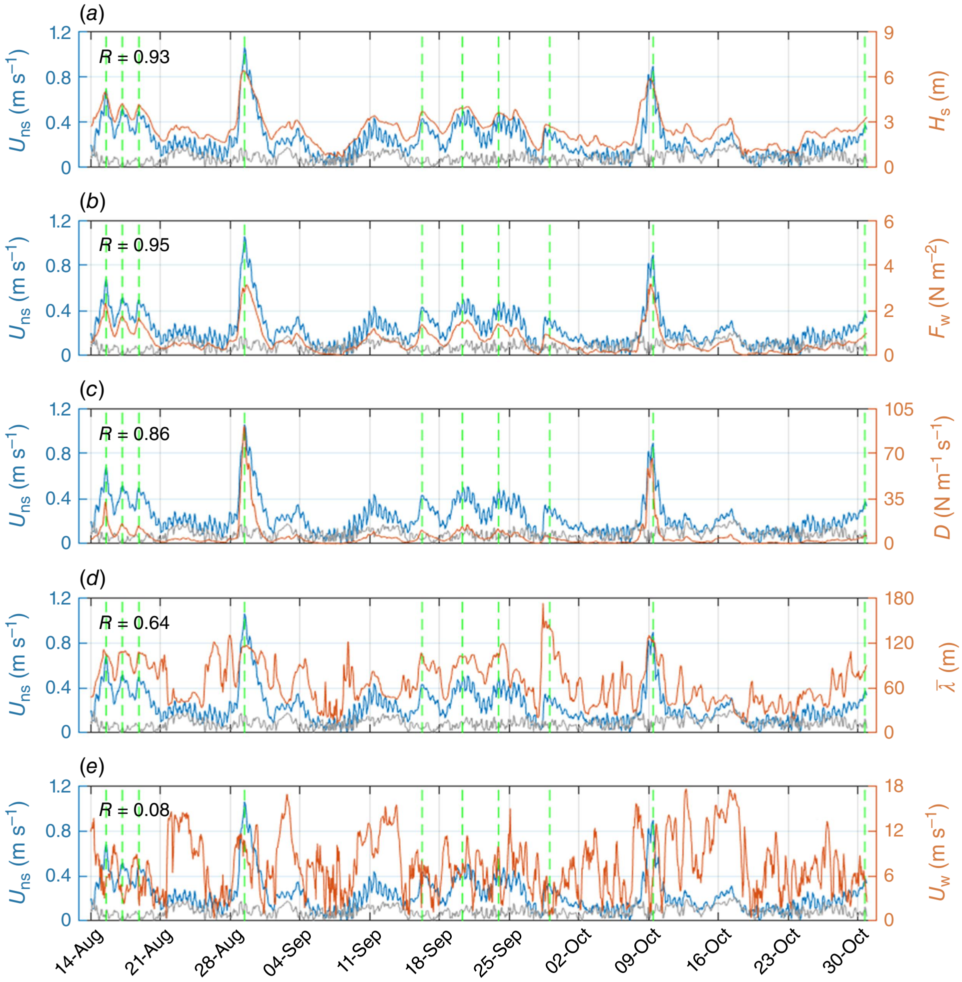

Fig. 8. Time series of near surface current speeds (U_{ns}; left-hand *y*-axes in all panels) from the wave-coupled simulation and (*a*) significant wave height (H_s), (*b*) wave-induced force (F_w), (*c*) wave energy dissipation rate (D), (*d*) mean spectral wavelength ($\bar{\lambda}$) and (e) wind speed (U_w) for the 2006 period. Near surface current and wind data are extracted from a point south-east of Robben Island (point C, Fig. 1). Significant wave height and mean spectral wavelength are extracted from a point 2.4 km to the west (point A, Fig. 1), whereas wave-induced force and wave energy dissipation rate are extracted from a point where the incident waves begin breaking (point B, Fig. 1). Correlation coefficients (R) are shown in the top left of each panel. In each case, the uncoupled current speeds are shown in grey (for comparison with the coupled speeds in blue). Green dashed lines indicate times at which the gyres identified and listed in Table 2 were at their peaks.

surface current speed at this site for the 2006 (2010) simulation. Links between bulk wave parameters and surface current speeds are clear, with their respective signals exhibiting a high degree of similarity. Surface currents at this point are strongly correlated with significant wave height ($R = 0.93$ for 2006, $R = 0.88$ for 2010), wave energy dissipation ($R = 0.86$ for 2006, $R = 0.84$ for 2010) and wavelength ($R = 0.64$ for 2006, $R = 0.64$ for 2010). Correlations with wavelength are consistent with those between flow speeds and estimates of mean wave period (T_{m-1}, $R = 0.54$ for 2006 and 0.56 for 2010; T_{m01}, $R = 0.58$ for 2006 and 0.60 for 2010; and T_{m02}, $R = 0.63$ for 2006 and 0.63 for 2010). Results for 2010 (not shown) are very similar. Weak correlation between current and wind speeds affirms the likelihood of waves being the dominant forcing of mean currents in this area.

Conspicuous peaks in wave conditions and current speeds on 29 August and 9 October (Fig. 8) and the failure of the uncoupled configuration to produce these flow events, underscore the importance of large wave events in forcing near-surface currents. These peaks correspond to two strong cases of the gyre discussed in Section 3.2 and shown in Fig. 4 and 5. Peaks in mean spectral wavelength during these events (Fig. 8*d*) confirm that it is likely that the swell band drives these strong flows. To assess the general dependency of surface currents on waves in Table Bay outside of

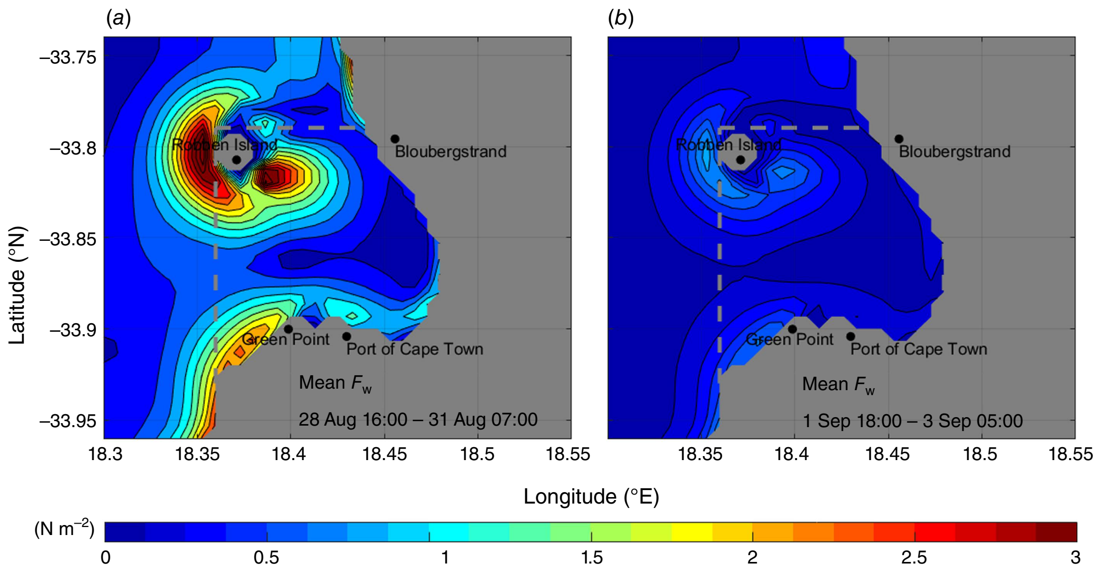

Fig. 9. Time-mean wave-induced force (F_w) during (a) a large wave event ($H_{s\ max} \approx 6\ m\ s^{-1}$) and (b) a strong south-easterly wind event ($W_{wind\ max} \approx 16\ m\ s^{-1}$). The dashed line indicates the bay interior for which means and maxima are reported in Section 3.

such events, spatial analysis of the wave-induced force was conducted. Time-mean wave-induced force was assessed for the simulation periods in their entirety, as well as for a high wave and high wind event (Fig. 9). This revealed that, although wave-induced forces are always in operation, they are several times larger during large wave events (when remotely forced, longer period waves such as swells are present) than when the wave spectrum is dominated by local wind waves. The mean wave-induced force F_w for the interior of the bay (dashed lines in Fig. 9) was 0.2 N m^{-2} for the 2006 simulation but reached as much as 12.6 N m^{-2} in places during the large wave event shown in Fig. 9a. This assessment was extended to a strong wind event (Fig. 9b) in order to assess the potential of wind waves in driving mean currents by whitecapping-related energy dissipation. Under strong winds but moderate wave conditions ($U_{wind\ max} \approx 16\ m\ s^{-1}$, $H_{s\ max} \approx 2.5\ m$), F_w reached a maximum of 2.5 N m^{-2}.

Wave energy dissipation due to bottom friction, depth-induced breaking and whitecapping is used to estimate the wave-induced forces driving currents as outlined in Section 2.1.4. Determining the relative contributions of each of the various wave energy dissipation mechanisms to this forcing objectively, however, requires dedicated focus and model setup and is beyond the scope of this study. For example, assessing whitecapping-related dissipation (S_{wc}) by postprocessing is problematic where spectral means (available model output) are used in the computation of dissipation source terms. van der Westhuysen et al. (2007) provides a comprehensive explanation in this regard. For example, where the whitecapping formulation is strongly dependent on mean spectral steepness ($\bar{s}$), the presence of swell in the wave field increases the mean spectral wavelength ($\bar{\lambda}$), thereby reducing $\bar{s}$ and, accordingly, S_{wc}. This is the reason for the move away from a spectral steepness-based formulation for whitecapping in the model, in favour of a saturation-based approach (van der Westhuysen et al. 2007) which is cognizant of local frequency. This formulation is shown to produce improved estimates of wave energy dissipation for wave fields with a mix of wind sea and swell, but S_{wc} is computed internally. Notwithstanding the limitations of $\bar{s}$-based approach, a rudimentary assessment of where whitecapping might be driving surface currents was made by postprocessing the model's bulk statistics output. The $\bar{s}$ can be computed as ka, where $k = 2\pi \div \bar{\lambda}$ is the wavenumber and $a = H_s \div 2$ is the amplitude above which a wave is assumed to break. Within Table Bay, $\bar{s}$ reached 0.3 during times of strong winds (north-westerly and south-easterly), which is within the range of critical values for whitecapping in deep water found in the literature (Toffoli et al. 2010; Perlin et al. 2013). In this regard, Table Bay was confirmed to constitute deep water for significant wave heights during strong wind events according to linear wave theory. Further, D values within the bay and away from areas of depth-induced breaking agree well with spectrally local estimates of Mulligan et al. (2008) of 0.1–10 N m^{-1} s^{-1} for wind speeds of 5–17 m s^{-1}, and spatial correlation analysis (not shown) returned moderate positive values (~0.5) of near surface current speed with D in the interior of the bay. This is borne out by moderate negative correlations with $\bar{\lambda}$ and positive correlation with s. These results provide a first guess regarding the importance of whitecapping in driving currents but should be considered using awareness of the limitations of a mean spectral steepness-based approach. Whitecapping is handled more appropriately internally in the model, using a spectrally local approach.

Along the south coast of Robben Island and to its south-east, and from there north-eastward towards the mainland (north of Bloubergstrand), strong positive spatial correlations (~0.9) between current speed and energy dissipation rate (not shown) are likely the result of depth-induced breaking of longer, higher energy waves. This is evidenced by concomitant strong positive correlations with H_s and $\bar{\lambda}$ in this area, and negligible (~0.1–0.3) correlations with $\bar{s}$ (bear in mind the steepness s of each of these longer waves will naturally increase ahead of breaking, potentially creating the expectation of a positive correlation with current speeds, but the *spectral mean* quantity $\bar{s}$ will remain relatively low when longer waves dominate the spectrum). Results for the point example in Fig. 8 provide further agreement with this. Time-series analysis like that shown in Fig. 8 was also performed for a point in the middle of the bay (point C, Fig. 1). For the 2006 simulation, correlations

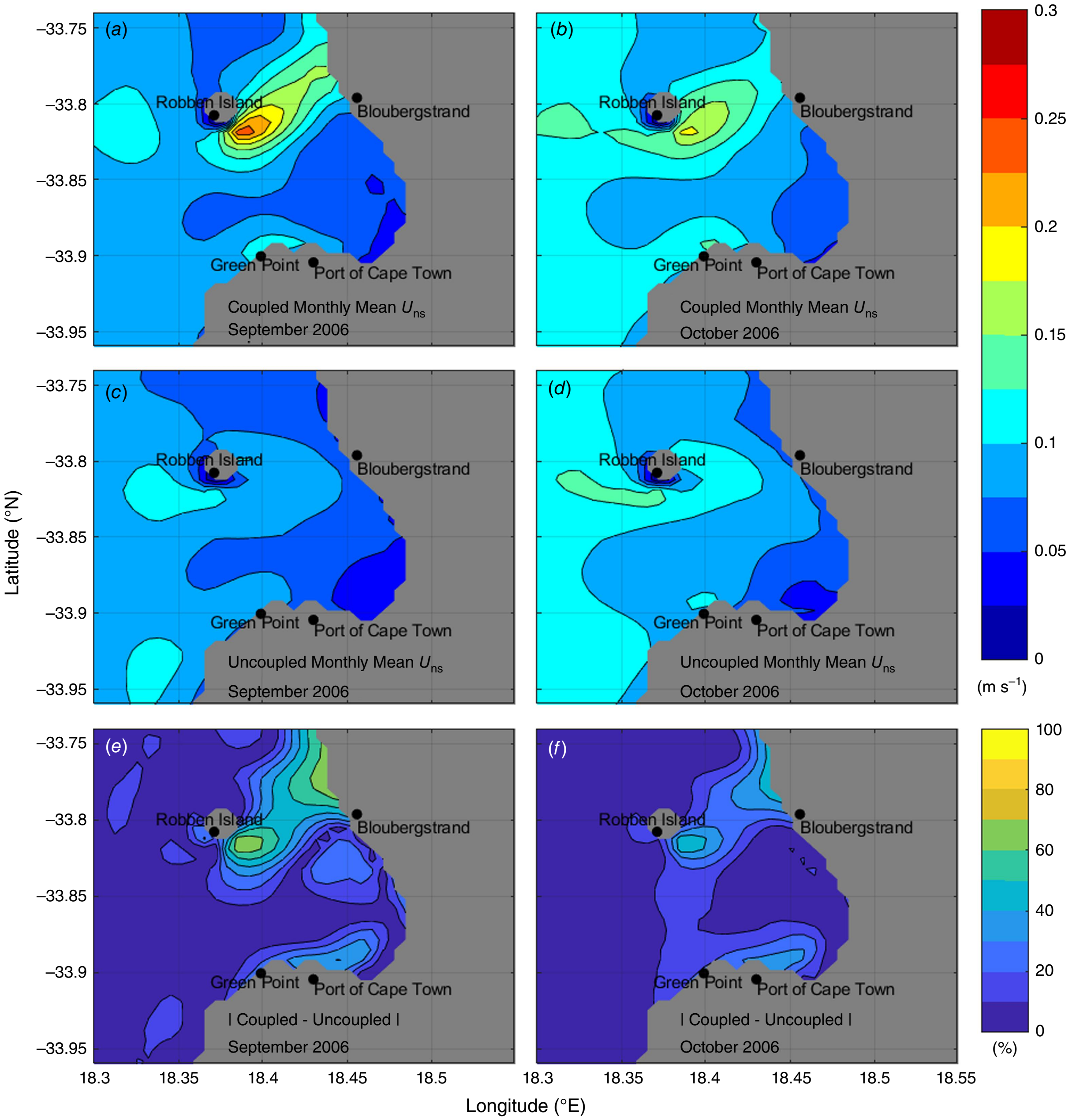

Fig. 10. Monthly mean near-surface current speed (U_{ns}) for (*a*, *c*, *e*) September and (*b*, *d*, *f*) October for the (*a*, *b*) wave-coupled and (*c*, *d*) wave-uncoupled simulations. (*e*, *f*) The percentage difference in monthly mean current speed between the coupled and uncoupled simulations.

here were 0.6 (0.6 in 2010) between surface current speeds and $\bar{s}$, and 0.56 (0.61 in 2010) between current and wind speed (both much higher than the case near Robben Island), whereas wave-driven forces were far lower than those near the island (maximum 0.62 in 2006 and 2010). This suggests that here the relative importance of wind as a driver of surface currents is increased, and where waves do induce forces, they are likely due to whitecapping-related energy dissipation (although as explained earlier, this forcing is negligible compared to depth-induced breaking forcing nearer the island).

Finally, the influence of wave-induced currents on the mean circulation of the bay was assessed. For the months of September and October in the 2006 and 2010 simulations, monthly mean flow speeds from the wave-coupled and -uncoupled configurations were compared. This revealed that, notwithstanding that the major contribution of wave-driven currents occurs during large wave events (with a smaller contribution during moderate and low wave conditions), these contributions were sufficient to modify the mean flow by 10–50% across much of the bay (Fig. 10). The effect is particularly pronounced south-east of Robben Island, and from there to the mainland north of Bloubergstrand (reaching 60–70% for the 2006 simulation). Naturally these findings apply within the confines of the time frames simulated in this study, but suggest that this is an important consideration for future investigation.

4. Conclusions

A coastal hydrodynamic model is employed to demonstrate the central importance of waves in driving surface currents in Table Bay. The model is able to reproduce the long-term and sub-daily velocity variability. A cyclonic circulation feature within the bay is identified and shown to be wave driven, dominating the circulation in the bay during large wave events. The feature is established primarily by the depth-induced breaking of high energy waves (such as swells) in the vicinity of Robben Island, significantly influencing the flow south-east of the island and near Bloubergstrand. The frequency of such events and the intensity of the currents they produce, combined with contributions from weaker wave-driven flows at other times resulted in the modification of the mean circulation for the months simulated. This suggests that wave-driven currents in Table Bay are relevant at both the event scale and for the mean circulation, although longer simulation periods are required to confirm this. Further, the classical notion that wave-driven currents are of primary importance only along the eastern margins of the bay, with wind being the primary driver elsewhere, is qualified by showing the importance of wave-driven flows throughout the bay, and that at times they may dominate the influence of wind. The occurrence of this feature in the model provides further motivation for enhanced observational capacity in this important embayment.

The results of a simple drift experiment using virtual drogues underscore the importance of including surface gravity wave forcing in all simulations of the circulation within Table Bay. In particular, modelling of currents for applications such as trajectory modelling for search and rescue are likely to be materially deficient in the absence of an appropriate handling of the contribution of waves to the Eulerian flow.

Given the vast activity within Table Bay and the multitude of human and natural interests, the findings of this study constitute an important consideration for future modelling and forecasting work. Future work would benefit greatly from longer simulations periods and more measurements of velocities within the bay.

References

Andrews DG, Mcintyre ME (1978) An exact theory of nonlinear waves on a Lagrangian-mean flow. *Journal of Fluid Mechanics* **89**, 609–646. doi:10.1017/s0022112078002773

Anxusani (2017) Skipper's lack of weather conditions awareness cause of Robben Island vessel incident: SAMSA. In *SAMSA*, 27 November 2017. Available at https://blog.samsa.org.za/2017/11/27/skippers-lack-of-weather-conditions-awareness-cause-of-robben-island-vessel-incident-samsa/ [Verified7 June 2021]

Ballance A, Ryan PG, Turpie JK (2000) How much is a clean beach worth? The impact of litter on beach users in the Cape Peninsula, South Africa. *South African Journal of Science* **96**, 210–213.

Barnes MA, Rautenbach C (2020) Toward operational wave–current interactions over the Agulhas Current System. *Journal of Geophysical Research: Oceans* **125**, e2020JC016321. doi:10.1029/2020JC016321

Battjes JA, Janssen JPFM (1978) Energy loss and set-up due to breaking of random waves. In 'Coastal Engineering 1978: 16th International Conference on Coastal Engineering', 27 August–3 September 1978, Hamburg, Germany. pp. 569–587. (American Society of Civil Engineers) doi:10.1061/9780872621909.034

Battjes JA, Stive MJF (1985) Calibration and verification of a dissipation model for random breaking waves. *Journal of Geophysical Research: Oceans* **90**(C5), 9159–9167. doi:10.1029/JC090iC05p09159

Battjes JA, Zitman TJ, Holthuijsen LH (1986) A re-analysis of the spectra observed in JONSWAP. In 'Coastal Engineering 1986: Proceedings of the 20th International Conference on Coastal Engineering', 9–14 November 1986, Taipei, Taiwan. pp. 17–26. (American Society of Civil Engineers) doi:10.1061/9780872626003.002

Benveniste J, Birol F, Calafat F, Cazenave A, Dieng H, Gouzenes Y, Legeais JF, Léger F, Niño F, Passaro M, Schwatke C, Shaw A (2020) Coastal sea level anomalies and associated trends from Jason satellite altimetry over 2002–2018. *Scientific Data* **7**, 357. doi:10.1038/s41597-020-00694-w

Booij N, Ris RC, Holthuijsen LH (1999) A third-generation wave model for coastal regions 1. Model description and validation. *Journal of Geophysical Research: Oceans* **104**, 7649–7666. doi:10.1029/98JC02622

Boyd AJ, Tromp BBS, Horstman DA (1985) The hydrology off the South African south-western coast between Cape Point and Danger Point in 1975. *South African Journal of Marine Science* **3**, 145–168. doi:10.2989/025776185784461225

Cats G (2014) Numerical modeling of wave–current interaction with the use of a two way coupled system. MSc thesis, TU Delft, Delft, Netherlands.

Council for Scientific and Industrial Research (1972*a*) Effects of proposed harbour developments on the Table Bay coastline. Report Volume I, Commercial report ME 1086/1, CSIR, Stellenbosch, South Africa.

Council for Scientific and Industrial Research (1972*b*) Effects of proposed harbour developments on the Table Bay coastline. Report Volume 2, Commercial report ME 1086/2, CSIR, Stellenbosch, South Africa.

Daniels T, Fearon G, Vilaplana A, Hewitson B, Rautenbach C (2022) On the importance of wind generated waves in embayments with complex orographic features – a South African case study. *Applied Ocean Research* **128**, 103355. doi:10.1016/j.apor.2022.103355

Dee DP, Uppala SM, Simmons AJ, Berrisford P, Poli P, Kobayashi S, Andrae U, Balmaseda MA, Balsamo G, Bauer P, Bechtold P, Beljaars ACM, van de Berg L, Bidlot J, Bormann N, Delsol C, Dragani R, Fuentes M, Geer AJ, Haimberger L, Healy SB, Hersbach H, Hólm EV, Isaksen L, Kållberg P, Köhler M, Matricardi M, Mcnally AP, Monge-Sanz BM, Morcrette JJ, Park BK, Peubey C, de Rosnay P, Tavolato C, Thépaut JN, Vitart F (2011) The ERA-Interim reanalysis: configuration and performance of the data assimilation system. *Quarterly Journal of the Royal Meteorological Society* **137**, 553–597. doi:10.1002/qj.828

Deltares (2020*a*) 'Delft3D FLOW – simulation of multi-dimensional hydrodynamic flows and transport phenomena, including sediments, User Manual.' (Deltares: Delft, Netherlands)

Deltares (2020*b*) 'Delft3D WAVE – simulation of short-crested waves with SWAN, User Manual.' (Deltares: Delft, Netherlands)

de Mendoza FP, Bonamano S, Martellucci R, Melchiorri C, Consalvi N, Piermattei V, Marcelli M (2018) Circulation during storms and dynamics of suspended matter in a sheltered coastal area. *Remote Sensing (Basel)* **10**, 602. doi:10.3390/rs10040602

de Mey P, Craig P, Davidson F, Edwards CCA, Ishikawa Y, Kindle JC, Proctor R, Thompson KR, Zhu J, The GODAE Coastal and Shelf Seas Working Group (CSSWG) Community (2009) Applications in coastal modeling and forecasting. *Oceanography* **22**, 198–205. doi:10.5670/oceanog.2009.79

de Vos M, Rautenbach C (2019) Investigating the connection between metocean conditions and coastal user safety: an analysis of search and rescue data. *Safety Science* **117**, 217–228. doi:10.1016/j.ssci.2019.03.029

de Vos M, Vichi M, Rautenbach C (2021) Simulating the coastal ocean circulation near the Cape Peninsula using a coupled numerical model. *Journal of Marine Science and Engineering* **9**, 359. doi:10.3390/jmse9040359

Dingemans MW, Radder AC, De Vriend HJ (1987) Computation of the driving forces of wave-induced currents. *Coastal Engineering* **11**, 539–563. doi:10.1016/0378-3839(87)90026-3

Elias EPL, Walstra DJR, Roelvink JA, Stive MJF, Klein MD (2000) Hydrodynamic validation of Delft3D with field measurements at Egmond. In 'Coastal Engineering 2000: Proceedings of the 27th International Conference on Coastal Engineering (ICCE)', 16–21 July 2000, Sydney, NSW, Australia. pp. 2714–2727. (American Society of Civil Engineers) Available at https://ascelibrary.org/action/showCitFormats?doi=10.1061%2F40549%28276%29212

Fossati M, Piedra-Cueva I (2013) A 3D hydrodynamic numerical model of the Río de la Plata and Montevideo's coastal zone. *Applied Mathematical Modelling* **37**, 1310–1332. doi:10.1016/j.apm.2012.04.010

Garcia M, Ramirez I, Verlaan M, Castillo J (2015) Application of a three-dimensional hydrodynamic model for San Quintin Bay, B.C., Mexico. Validation and calibration using OpenDA. *Journal of Computational and Applied Mathematics* **273**, 428–437. doi:10.1016/j.cam.2014.05.003

Gerritsen H, De Goede ED, Platzek FW, van Kester JATM, Genseberger M, Uittenbogaard RE (2008) 'Validation Document Delft3D- FLOW, a software system for 3D flow simulations', 1.1. edn. (Deltares: Delft, Netherlands)

Gill A (1982) 'Atmosphere-Ocean Dynamics', 1st edn. (Academic Press: London, UK)

Hahmann AN, Lennard C, Badger J, Vincent CL, Kelly MC, Volker PJH, Argent B, Refslund J, Andrea N, Louise C, Mark C, Patrick JH (2014) 'Mesoscale modeling for the Wind Atlas of South Africa (WASA) project.' (Department of Wind Energy E Report 2014: Roskilde, Denmark) doi:10.13140/RG.2.1.3735.6887

Hasan GMJ, van Maren DS, Ooi SK (2016) Hydrodynamic modeling of Singapore's coastal waters: nesting and model accuracy. *Ocean Modelling* **97**, 141–151. doi:10.1016/j.ocemod.2015.09.002

Jones DW, Olsonbaker JI (2005) Determining the information needs of Puget Sound boaters. *Proceedings of the Human Factors and Ergonomics Society Annual Meeting* **49**, 553–556. doi:10.1177/154193120504900372

Jury MR (1984) Wind shear and differential upwelling along the South Western tip of Africa. PhD thesis, University of Cape Town, Cape Town, South Africa.

Lamb H (1993) 'Hydrodynamics', 6th edn. (Cambridge University Press: New York, NY, USA)

Lane A (1989) 'The heat balance of the North Sea.' (Proudman Oceanographic Laboratory: Birkenhead, UK)

Lesser GR, Roelvink JA, van Kester JATM, Stelling GS (2004) Development and validation of a three-dimensional morphological model. *Coastal Engineering* **51**, 883–915. doi:10.1016/j.coastaleng.2004.07.014

Longuet-Higgins MS, Stewart Rw (1964) Radiation stresses in water waves; a physical discussion, with applications. *Deep Sea Research and Oceanographic Abstracts* **11**, 529–562. doi:10.1016/0011-7471(64)90001-4

Madsen OS, Poon YK, Graber HC (1988) Spectral wave attenuation by bottom friction: theory. In 'Coastal Engineering 1988: 21st International Conference on Coastal Engineering', 20–25 June 1988, Costa del Sol-Malaga, Spain. pp. 492–504. (American Society of Civil Engineers) doi:10.1061/9780872626874.035

Metzger EJ, Helber RW, Hogan PJ, Posey PG, Thoppil PG, Townsend TL, Wallcraft AJ (2017) Global Ocean Forecast System 3.1 Validation Testing. NRL/MR/7320--17-9722, Naval Research Laboratory, Stennis Space Center, MI, USA.

Mulligan RP, Hay AE, Bowen AJ (2008) Wave-driven circulation in a coastal bay during the landfall of a hurricane. *Journal of Geophysical Research: Oceans* **113**, C05026. doi:10.1029/2007JC004500

Mulligan RP, Hay AE, Bowen AJ (2010) A wave-driven jet over a rocky shoal. *Journal of Geophysical Research: Oceans* **115**, C10038. doi:10.1029/2009JC006027

Munien S, Gumede A, Gounden R, Bob U, Gounden D, Perry NS (2019) Profile of visitors to coastal and marine tourism locations in cape town, South Africa. *Geojournal of Tourism and Geosites* **27**, 1134–1147. doi:10.30892/gtg.27402-421

Nguyen DT, Reniers AJHM, Roelvink D (2021) Relationship between three-dimensional radiation stress and Vortex-Force representations. *Journal of Marine Science and Engineering* **9**, 791. doi:10.3390/jmse9080791

Peng Z, Bradon J (2016) 3-D Comprehensive hydrodynamic modelling in the Arabian Gulf. *Journal of Coastal Research* **75**, 547–551. doi:10.2112/si75-110.1

Perlin M, Choi W, Tian Z (2013) Breaking waves in deep and intermediate waters. *Annual Review of Fluid Mechanics* **45**, 115–145. doi:10.1146/annurev-fluid-011212-140721

Potgieter L, Goedhals-Gerber LL, Havenga J (2020) Risk profile of weather and system-related port congestion for the Cape Town container terminal. *Southern African Business Review* **24**, 6149. doi:10.25159/1998-8125/6149

Putzu S, Enrile F, Besio G, Cucco A, Cutroneo L, Capello M, Stocchino A (2019) A reasoned comparison between two hydrodynamic models: Delft3D-Flow and ROMS (regional oceanic modelling system). *Journal of Marine Science and Engineering* **7**, 464. doi:10.3390/JMSE7120464

Quick AJR, Roberts MJ (1993) Table Bay, Cape Town, South Africa: synthesis of available information and management implications. *South African Journal of Science* **89**, 276–287.

Rautenbach C, Barnes MA, Wang DW, Dykes J (2020*a*) Southern african wave model sensitivities and accuracies. *Journal of Marine Science and Engineering* **8**, 773. doi:10.3390/jmse8100773

Rautenbach C, Daniels T, de Vos M, Barnes MA (2020*b*) A coupled wave, tide and storm surge operational forecasting system for South Africa: validation and physical description. *Natural Hazards* **103**, 1407–1439. doi:10.1007/s11069-020-04042-4

Rey AJM, Mulligan RP (2021) Influence of hurricane wind field variability on real-time forecast simulations of the coastal environment. *Journal of Geophysical Research: Oceans* **126**, e2020JC016489. doi:10.1029/2020jc016489

Ris RC, Holthuijsen LH, Booij N (1999) A third-generation wave model for coastal regions. *Journal of Geophysical Research: Oceans* **104**, 7667–7681. doi:10.1029/1998JC900123

Roelvink JA, Van Banning GKFM (1995) Design and development of DELFT3D and application to coastal morphodynamics. *Oceanographic Literature Review* **11**, 925.

Rogers WE, Kaihatu JM, Hsu L, Jensen RE, Dykes JD, Holland KT (2007) Forecasting and hindcasting waves with the SWAN model in the Southern California Bight. *Coastal Engineering* **54**, 1–15. doi:10.1016/j.coastaleng.2006.06.011

Schumann EH, Perrins L-A (1982) Tidal and inertial currents around South Africa. In 'Proceedings of 18th Conference on Coastal Engineering', 14–19 November 1982, Cape Town, South Africa. (Ed. BL Edge) pp. 2562–2580. (American Society of Civil Engineers) doi:10.1061/9780872623736.156

Sembiring L, van Ormondt M, van Dongeren A, Roelvink D (2015) A validation of an operational wave and surge prediction system for the Dutch coast. *Natural Hazards and Earth System Sciences* **15**, 1231–1242. doi:10.5194/nhess-15-1231-2015

Skamarock WC, Klemp JB, Dudhia JB, Gill DO, Barker DM, Duda MG, Huang X-Y, Wang W, Powers JG (2008) 'A description of the Advanced Research WRF Version 3.' (National Center for Atmospheric Research: Boulder, CO, USA) doi:10.5065/D68S4MVH

Stelling GS (1983) On the construction of computational methods for shallow water flow problems. PhD thesis, TU Delft, Delft, Netherlands.

Swett RA, Sidman C, Fik T, Watkins R, Ouellette P (2011) Evaluating boating safety risk in intracoastal waterways. *Coastal Management* **39**, 613–627. doi:10.1080/08920753.2011.616661

Thomas TJ, Dwarakish GS (2015) Numerical wave modelling – a review. *Aquatic Procedia* **4**, 443–448. doi:10.1016/j.aqpro.2015.02.059

Toffoli A, Babanin A, Onorato M, Waseda T (2010) Maximum steepness of oceanic waves: field and laboratory. *Geophysical Research Letters* **37**, L05603. doi:10.1029/2009GL041771

Tyson PD, Garstang M, Swap R, Kâllberg P, Edwards M (1996) An air transport climatology for subtropical Southern Africa. *International Journal of Climatology* **16**, 265–291. doi:10.1002/(SICI)1097-0088(199603)16:3<265::AID-JOC8>3.0.CO;2-M

Van Ballegooyen RC (2007) 'Ben Schoeman Dock Berth Deepening Project Integrated Marine Impact Assessment Study.' (Council for Scientific and Industrial Research: Stellenbosch, South Africa)

van der Westhuysen AJ (2007) Advances in the spectral modelling of wind waves in the nearshore. PhD thesis, TU Delft, Delft, Netherlands.

van der Westhuysen AJ, Zijlema M, Battjes JA (2007) Nonlinear saturation-based whitecapping dissipation in SWAN for deep and shallow water. *Coastal Engineering* **54**, 151–170. doi:10.1016/j.coastaleng.2006.08.006

Van Ieperen MP (1971) Hydrology of Table Bay. Final report, Department of Oceanography, University of Cape Town, Cape Town, South Africa.

Veitch J, Rautenbach C, Hermes J, Reason C (2019) The Cape Point wave record, extreme events and the role of large-scale modes of climate variability. *Journal of Marine Systems* **198**, 103185. doi:10.1016/j.jmarsys.2019.103185

Williams JJ, Esteves LS (2017) Guidance on setup, calibration, and validation of hydrodynamic, wave, and sediment models for shelf seas and estuaries. *Advances in Civil Engineering* **2017**, 5251902. doi:10.1155/2017/5251902

Zubier K, Panchang V, Demirbilek Z (2003) Simulation of waves at duck (North Carolina) using two numerical models. *Coastal Engineering Journal* **45**, 439–469. doi:10.1142/S0578563403000853

Data availability. The data utilised in this study are available upon request of the corresponding author.

Conflicts of interest. The authors declare that they have no conflicts of interest.

Declaration of funding. This work was partially supported by the National Research Foundation of South Africa (grant number 118754) from the South Africa–Norway cooperation on ocean research including blue economy, climate change, the environment and sustainable energy (SANOCEAN) project.

Acknowledgements. The authors would like to thank the Transnet National Ports Authority (TNPA) for the provision of current and wave measurement data, the South African National Hydrographic Office (SANHO) for the use of water level and bathymetric data, the Council for Scientific and Industrial Research (CSIR) for the use of current measurement data and the Climate Systems Analysis Group (CSAG) for the use of the WASA wind forcing data.

Author affiliations

[A]Marine Research Unit, South African Weather Service, Cape Town, Western Cape, South Africa.

[B]Department of Oceanography, University of Cape Town, Cape Town, Western Cape, South Africa.

[C]Marine and Antarctic Research Centre for Innovation and Sustainability (MARIS), University of Cape Town, Cape Town, Western Cape, South Africa.

[D]Coastal and Estuarine Processes, National Institute for Water and Atmospheric Research, Hamilton, Waikato, New Zealand.

[E]Institute for Coastal and Marine Research, Nelson Mandela University, Port Elizabeth, Eastern Cape, South Africa.